Supporting Information

Hydrogen-Type Binding Sites in Carbonaceous Electrodes for Rapid Lithium Insertion

Devin McGlamery, Charles McDaniel, Wei Xu, and Nicholas P. Stadie*

Department of Chemistry & Biochemistry, Montana State University, Bozeman, Montana 59717, United States

*Email: nstadie@montana.edu

Contents:

1.	Direct Synthesis of PAH-Derived Carbons	s2
2.	Synthesis of ZTC	s2
3.	Powder XRD	s3
4.	Raman Spectroscopy	s5
5.	Surface Area Measurements	s6
6.	Elemental Analysis	s7
7.	Atomistic Depictions	s8
8.	Electrochemical Characterization	s8
9.	Site Type Distribution Calculations	s10
10.	Energy and Power Calculations	s11
11.	Structural Characterization of PAH-Derived Carbons	s11
12.	Electrochemical Characterization of PAH-Derived Carbons	s13
13.	Further Electrochemical Characterization of Primary Materials	s14
14.	Supporting References	s15

1. Direct Synthesis of PAH-Derived Carbons

The primary materials investigated in the present work were synthesized by the pyrolysis of benzene (Sigma-Aldrich, anhydrous 99.8%), naphthalene (Acros Organics, 99+%), pyrene (Acros Organics, 98%), or coronene (Acros Organics, 95%) under inert conditions at 800 °C to produce Ben800, Nap800, Pyr800, and Cor800, respectively. A typical synthesis of Cor800 was performed by adding 420 mg of coronene to a 30 mL quartz ampule within an argon-filled glovebox (<0.5 ppm O_2, <0.5 ppm H_2O). The ampule was then temporarily sealed with a custom Swagelok Ultra-Torr Schlenk line adapter and removed from the glovebox. At this point the ampule contents were frozen by immersing the ampule in liquid nitrogen and evacuation to 10^{-3} mbar within 30 s. In this state the ampule was flame-sealed with an oxyhydrogen torch. The sealed ampule was then placed in the center of a chamber furnace (RWF 12/13, Carbolite Gero Ltd.) and heated to 800 °C via a 1 °C min^{-1} ramp. The set temperature was held for 1 h and then allowed to gradually cool to ambient temperature. The ampule was scored with a diamond-bladed saw, the outside washed with deionized water and dried, then snapped open within a nitrile rubber enclosure, releasing the overpressure of gaseous byproducts into a fume hood. The material was collected as large, lustrous flakes; the flakes of Ben800 were quite thin and flexible and this transitioned to thicker, almost glassy flakes for Cor800. A portion of each product was hand-ground for 10 min with a mortar and pestle to produce homogeneous powders for XRD and electrochemical characterization.

2. Synthesis of ZTC

Zeolite-templated carbon (ZTC) was synthesized via a two-step method, where the NaY zeolite template (4 g, HSZ 320NAA, Tosoh Corp.) was degassed in a glass oven (B-585, Büchi) at 300 °C for 24 h under oil-free vacuum (<2 × 10^{-3} mbar). The dried zeolite was then transferred under inert conditions into a 2-neck round-bottom flask and impregnated with 40 mL of furfuryl alcohol (FA, 99%, Aldrich) via syringe. The mixture was stirred under passive vacuum at room temperature for 24 h, after which the impregnated

solid was collected by vacuum filtration in air, washed three times with 10 mL aliquots of mesitylene (97%, Aldrich), and dried under suction on the filter frit for 10 min. The impregnated and washed zeolite was then split equally into two alumina boats (10 × 30 × 107 mm) and inserted into a quartz tube (ø 45 mm) installed in a horizontal furnace (HST 12/600, Carbolite Gero Ltd.). The tube was purged via dry argon flow (200 sccm) at ambient pressure. Polymerization of FA inside the zeolite pores was achieved by heating to 80 °C at 5 °C min^{-1} under flowing dry argon for 24 h. The poly-FA was then carbonized by heating to 700 °C at 5 °C min^{-1}, after which further carbon introduction was achieved via chemical vapor deposition (CVD) at 700 °C under flowing 7 mol% propylene in argon (99.99% propylene in 99.999% argon) at 200 sccm. After ambient-pressure CVD for 5 h, the gas flow was returned to dry argon at 200 sccm. An annealing step was performed by heating the zeolite-carbon composite up to 900 °C at 5 °C min^{-1} and held for an additional 3 h. The system was allowed to cool overnight, the gas flow was stopped, and the zeolite-carbon composite was collected. The zeolite template was removed via three sequential dissolutions in 35 mL of aqueous hydrofluoric acid (HF, 48-51%, Thermo Scientific), followed by centrifugation and three washes with distilled water. The final ZTC product was then dried in air at 40 °C.

3. Powder XRD

X-ray diffraction (XRD) was performed on the hand-ground samples using a powder diffractometer (D8 ADVANCE, Bruker) in reflection geometry equipped with a Cu $K\alpha_{1,2}$ radiation source (λ = 1.54 Å). The sample was placed in the 25 mm diameter well of a circular sample holder, and the excess material was removed to produce a level sampling surface. The sample was rotated at 15 rev min^{-1} and sampled in 0.02° increments for 0.3 s each from 10° to 60°.

Analysis of the as-measured XRD patterns was accomplished by direct subtraction of the background based on an identical experiment performed without any sample. The resulting pattern was then fitted to

the combination of a linear background, a single Lorentzian for the (002) reflection, and two Lorentzian functions for the (10l) region comprised of the (100) and (101) reflections of crystalline graphite.

The peak center of the (002) reflection was related to the d-spacing (d) via Bragg's law, **Equation 1**, and the full-width at half-maxima (FWHM) of the (002) and (10l) reflections were used to estimate the crystallite size along the c and a axes ($\mathrm{L_c}$ and $\mathrm{L_a}$, respectively) via the Scherrer equation, **Equation 2**. The d-spacing and Scherrer size estimates based on the (002) reflection correspond to c-axis (layer-to-layer) ordering whereas those based on the (10l) reflections correspond to a-axis (in-plane) ordering.[1]

$$\mathrm{d} = \frac{1.54\ \text{Å}}{2\sin\theta} \tag{1}$$

$$\mathrm{L} = \frac{0.9\left(1.54\ \text{Å}\right)}{(\mathrm{FWHM})\cos\theta} \tag{2}$$

The FWHM in the Scherrer equation corresponds to the width of the reflection in 2θ expressed in radians.

4. Raman Spectroscopy

Room temperature measurements were conducted with a Raman spectrometer (LabRAM HR Evolution, Horiba Scientific Ltd.) equipped with a confocal microscope and a 532 nm (2.33 eV) frequency-doubled Nd:YAG laser with an incident power of 45 mW.

The region containing peaks associated to the D and G modes in each Raman spectrum were fitted using a previously established method based on the combination of a Lorentzian and a Breit-Wigner-Fano (BWF) lineshape.[2,3] The main D peak was fitted to a single Lorentzian and the low frequency shoulder of the D peak was fitted to another Lorentzian to account for hydrogen edge character and denoted as (*C–H). The G peak was fitted to a single BWF, and the baseline was approximated by a linear background, as shown in **Figure S1**. The combination of two Lorentzian functions and a BWF provided a profile with minimal fitting parameters that could effectively fit the Raman spectrum of the wide range of carbon materials with varying hydrogen content explored in this work. The BWF lineshape is given by:

$$I(\omega) = I_o \frac{[1 + (\omega - \omega_o/Q\Gamma)]^2}{1 + [(\omega - \omega_o)/\Gamma]^2} \quad (3)$$

where I_o is the peak intensity, ω_o is the peak position, Γ is the FWHM, and Q is the BWF coupling coefficient. A negative Q value tails the BWF toward lower frequency and helps accounts for residual intensity between the D and G peaks. Due to the asymmetry of the BWF lineshape, ω_o does not lie at the frequency of the peak maximum (ω_{max}) as in a simple Lorentzian or Gaussian function. To correct for this, the following equation was applied to determine ω_{max}:

$$\omega_{max} = \omega_o + \frac{\Gamma}{2Q} \quad (4)$$

Since Q is negative, ω_{max} lies at a lower frequency than ω_o.

FWHM(D) and FWHM(G) were determined based on FWHM of the Lorentzian associated with the D Peak and BWF fits, respectively. Pos(D) was determined based on ω_o of the Lorentzian associated with the D Peak, and Pos(G) was determined based on ω_{max} of the BWF associated with the G peak by applying **Equation 4**.

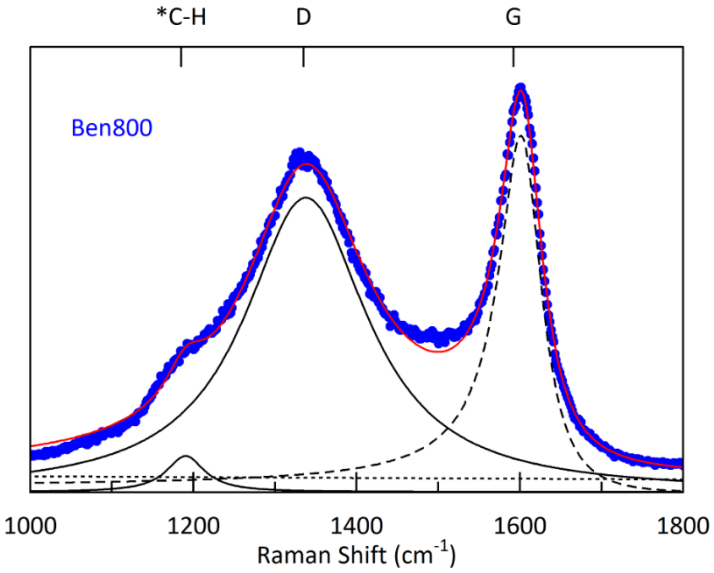

Figure S1. Representative fitting profile for the Raman spectrum of graphitic carbon. One Lorentzian (*C–H) is used to account for hydrogen edge character, a second Lorentzian (D) accounts for the D mode, and a BWF lineshape (G) accounts for the G mode.

5. Surface Area Measurements

The surface area of each sample was determined by applying Brunauer-Emmett-Teller (BET) analysis to N_2 adsorption equilibria measured using a volumetric apparatus (3Flex, Micromeritics Corp.). In each experiment, 200-300 mg of sample was loaded and degassed at 130 °C for 180 min, and then adsorption and desorption equilibria were measured at liquid nitrogen temperature (~77 K). N_2 adsorption isotherms of AG20, Cor800, Super P, and ZTC are shown in **Figure S2**; the corresponding pore size distributions via non-local density functional theory (NLDFT) methods are shown in **Figure S3**.

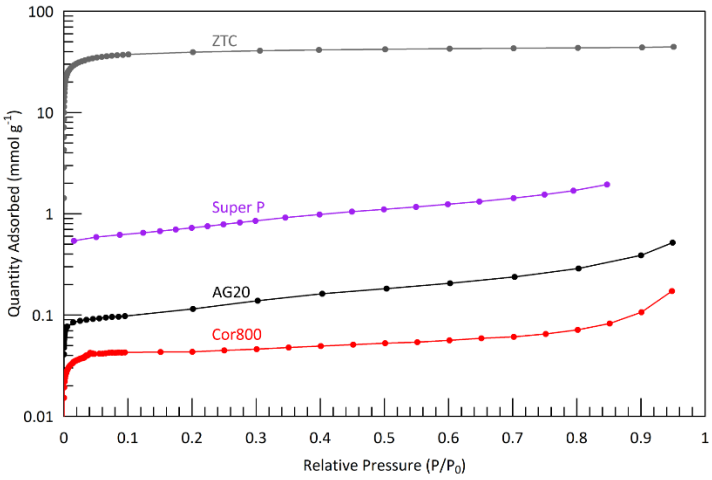

Figure S2. Equilibrium adsorption isotherms of N_2 on ZTC, Super P, AG20, and Cor800 at ~77 K.

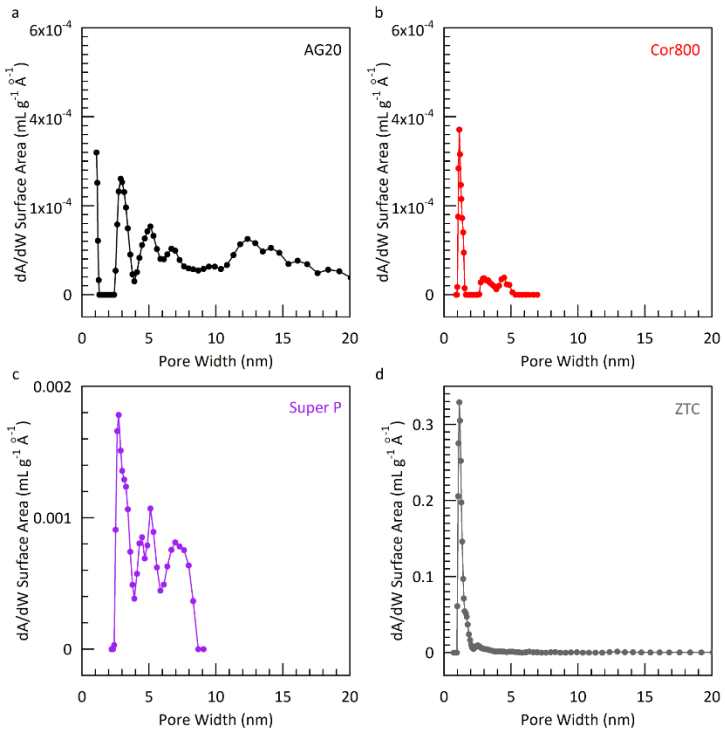

Figure S3. N_2-accessible pore size distributions of (a) AG20, (b) Cor800, (c) Super P, and (d) ZTC.

6. Elemental Analysis

The CHO elemental composition of each material was determined in triplicate using flame combustion (Atlantic Microlab, Inc.), and is reported herein as the average and converted to atomic fractions.

7. Atomistic Depictions

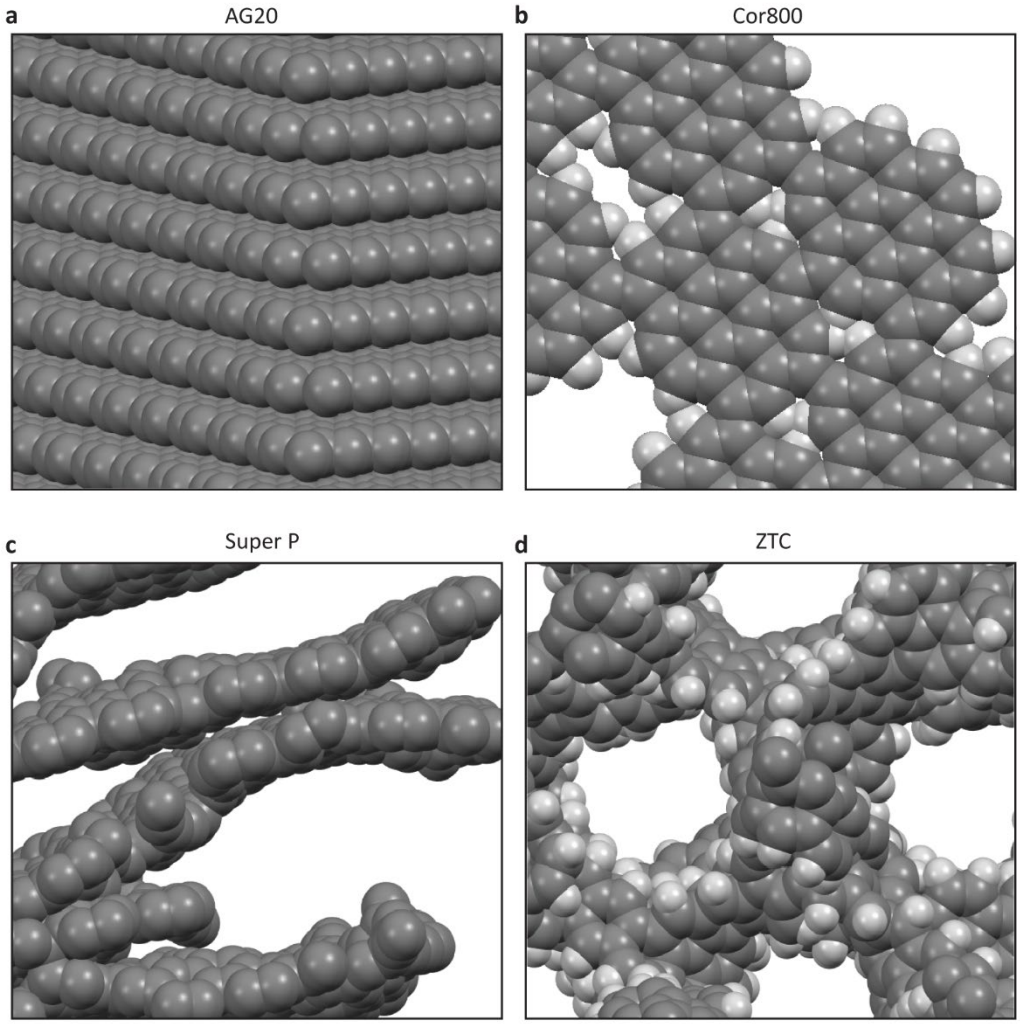

Figure S4. Atomistic depictions of (a) graphite (AG20), (b) graphitic carbon with hydrogen-type sites (Cor800), (d) hard carbon (Super P), and (e) ordered porous carbon with no stacking (ZTC).

8. Electrochemical Characterization

The working electrode slurry was comprised of 80 wt.% active materials, 10 wt.% Super P as a conductive additive, and 10 wt.% polyvinylidene fluoride (PVDF) as a binder, with a total loading mass of 1.5-2.0 mg cm^{-2} cast onto copper foil; the active mass loading was 1.2-1.6 mg cm^{-2}. The electrode sheet was first dried in a forced-air oven at 80 °C for 12 h and then transferred to a vacuum oven and dried overnight at 100 °C to remove any moisture and solvent. Coin cells (316 stainless steel, size 2032, Xiamen AOT Electronics

Technology Co.) were assembled in an argon-filled glovebox, with a lithium chip used as the counter and reference electrode, and with a glass microfiber separator (GF/D grade, catalogue number 1823–257, Whatman). The electrolyte used was 1.2 M lithium hexafluorophosphate ($LiPF_6$) in a mixture of ethylene carbonate and ethyl methyl carbonate (EC/EMC, 3:7 by weight) with 2 wt.% fluoroethylene carbonate (FEC) as an additive. Galvanostatic charge and discharge (GCD) profiles were measured using a battery cycler (CT30001A, Landt Instruments) at a constant temperature of 25.0 °C. All cells underwent a conditioning protocol comprising five formation cycles at 0.2 C to establish a stable initial capacity (omitted in **Figure 3b**). Additional cycles were then carried out at higher current rates (1 C, 2 C, 4 C, 6 C, 8 C, 10 C, 20 C, 40 C, 60 C, and 80 C) to evaluate rapid-charging performance and rate capability. The charge step was performed using a constant current constant voltage (CCCV) protocol wherein a constant current was first applied (according to an idealized capacity of 370 mAh g^{-1}) until the cutoff voltage was reached, and then the voltage was held constant until the total charging time limit was reached (as determined by the desired practical C rate). For example, during a CCCV charge step at 60 C, the cell was first charged at 22.2 A g^{-1} until the cutoff voltage was reached and then further charged at the cutoff voltage for the remaining time expected in a 60 C charge (taking 1 min total). The discharge step was always performed using a constant current (CC) protocol. The reversible discharge capacity was reported as normalized per mass of active material. Cyclic voltammetry (CV) was performed on separate cells using a dedicated potentiostat (VersaSTAT 4-450, Princeton Applied Research).

9. Site Type Distribution Calculations

The total electrochemical capacity (Q_{tot}) of each material was assessed as associated with a combination of three types of lithiation sites: capacitive surface adsorption (Q_A), faradaic interlayer intercalation (Q_I), and H-type sites (Q_H), as shown in **Figure 3e**. The distribution of these sites within each material was estimated by coupling information gleaned from GCD and CV experiments conducted under equivalent rate conditions. The following equations were used to estimate the contribution from each site type:

$$Q_A(\text{mAh g}^{-1}) = SA(\text{m}^2\ \text{g}^{-1}) \times 0.2839\ (\text{mAh m}^{-2}) \times F_{rate} \quad (5)$$

$$Q_I(\text{mAh g}^{-1}) = \left(Q_{tot}\,(\text{mAh g}^{-1}) - Q_A(\text{mAh g}^{-1})\right) \times \alpha_I \quad (6)$$

$$Q_H(\text{mAh g}^{-1}) = \left(Q_{tot}\,(\text{mAh g}^{-1}) - Q_A(\text{mAh g}^{-1})\right) \times \alpha_H \quad (7)$$

$$\alpha_I + \alpha_H = 1 \quad (8)$$

In Equation 5, SA is the N_2-accessible surface area of the material (in $m^2\ g^{-1}$) and the factor 0.2839 (in mAh m^{-2}) is the theoretical maximum capacity per unit surface area, assuming that a single-sided graphene sheet (1310 $m^2\ g^{-1}$) can be lithiated up to 372 mAh g^{-1} (LiC_6). The adsorption capacity fading due to rate (a small but observable effect) is accounted for by F_{rate}, a "fade factor" that is based on the observed capacity fading of ZTC as a function of current rate. In Equations 6 and 7, Q_{tot} is the total reversible discharge capacity of the material in mAh g^{-1}, as determined via GCD analysis at the corresponding rate. The weighting factors $\alpha_I$and α_H are fractions between 0 and 1 that are determined by integrating the oxidative CV profile of the relevant material (the delithiation scan typically had higher resolution with respect to the different features present) and assigning the total integrated area to two peaks, one for intercalation (at low potentials) and one for H-type sites (at ~0.5 V). The CV scan rate was chosen to be an equivalent overall delithiation rate to that for the corresponding GCD experiment. Note: only the Cor800 was treated by this entire method since Super P and AG20 were assessed as exhibiting only capacitive and intercalative storage ($\alpha_H = 0$), and ZTC was assessed as exhibiting only capacitive storage ($Q_{tot} = Q_A$).

10. Energy and Power Calculations

Specific energy and specific power with respect to the active materials investigated herein were used to generate a Ragone plot showing charged power as a function of discharged energy (**Figure 3d**). Specific energy (E, in Wh kg^{-1}) was determined as:

$$\mathrm{E} = \mathrm{Q} \times \left(\mathrm{V}_{\mathrm{cat,theo}} - \mathrm{V}_{\mathrm{an,avg}}\right) \quad (9)$$

where Q is the average measured discharge capacity over the last five cycles of a given charging rate step (in mAh g^{-1}, as shown in **Figure 3b**), $\mathrm{V}_{\mathrm{cat,theo}}$ is a fixed theoretical value set herein by the typical (de)lithiation potential of either lithium-iron phosphate (LFP) or nickel-manganese-cobalt oxide (NMC) used as a cathode (3.4 or 4.2 V vs. Li/Li^+, respectively), and $\mathrm{V}_{\mathrm{an,avg}}$ is the average measured half-cell voltage (also averaged over the last five cycles of a given step). The corresponding specific power (P, in W kg^{-1}) was then calculated using:

$$\mathrm{P} = \mathrm{I} \times \left(\mathrm{V}_{\mathrm{cat,theo}} - \mathrm{V}_{\mathrm{an,avg}}\right) \quad (10)$$

where I is the current rate during the charge step in mA g^{-1}.

It must be stressed that the calculated specific energy and specific power determined in this work are based on the mass of the active material alone and not the mass of a full-cell assembly.

11. Structural Characterization of PAH-Derived Carbons

XRD patterns of Ben800, Nap800, Pyr800, and Cor800 are shown in **Figure S5a**. The XRD patterns of all PAH-derived materials can be indexed to the hexagonal graphite unit cell, with a broad (002) reflection that shifts from $2\theta = 24.9°$ for Ben800 up to 26.2° for Cor800. The FWHM of the (002) reflection of these materials decreases from 6.34° in 2θ for Ben800 down to 3.49° for Cor800. The observed width of these peaks is attributed to Scherrer broadening and the Scherrer crystallite size in the c-axis was determined according to **Equation 2**. A summary of the structural properties of the PAH-derived carbons is shown in

Table S1. The crystallite size in the c-axis as well as the interlayer distance were found to be correlated to the ring count of the PAH precursor molecule: 1 for benzene, 2 for naphthalene, 4 for pyrene, and 7 for coronene. The correlation between improved crystallinity and PAH ring count is attributed to the significant intermolecular π-π stacking forces present in these planar aromatic molecules. A proxy for assessing the strength of these van der Waals interactions is the melting point of the PAH precursor (e.g., benzene at -5°C and coronene at 412 °C, respectively). As a result, larger precursors lead to an enhancement of c-axis stacking and larger crystallites along the c-axis due to the intrinsic π-π stacking strength of the pyrolyzed fragments. A weaker (10l) family of XRD reflections can also be observed at 2θ = 43°, a convolution of the (100) and (101) reflections of the hexagonal graphite unit cell. This reflection mainly corresponds to ordering along the a-axis of the graphitic unit cell and is found to be relatively unaffected by precursor size.

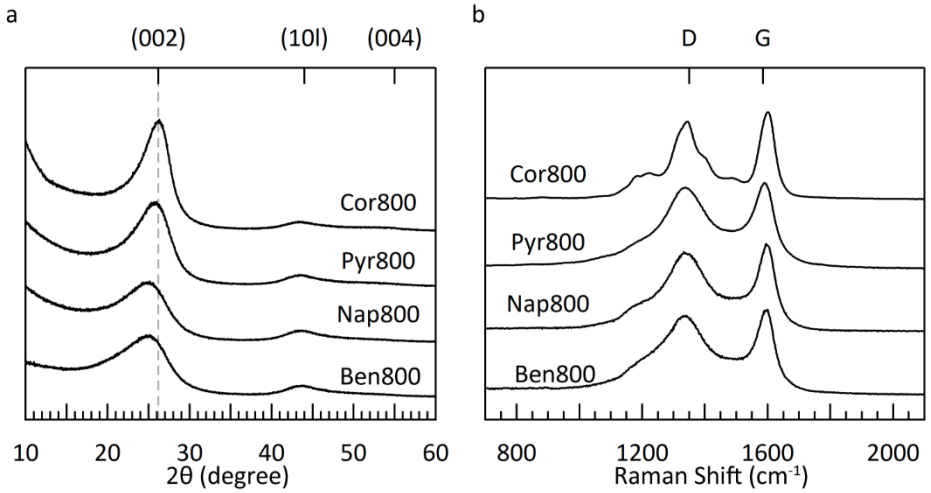

Figure S5. (a) XRD and (b) Raman spectra (collected using a 532 nm excitation source) of Ben800, Nap800, Pyr800, and Cor800.

The Raman spectra of Ben800, Nap800, Pyr800, and Cor800 are shown in **Figure S5b**. The improved crystallinity achieved with larger precursors observed in XRD is also evident in the Raman spectrum by a narrowing of the G peak. The G mode frequency decreases from 72 cm^{-1} for Ben800 to 53

cm^{-1} for Cor800, corresponding to a more homogeneous distribution of sp^2 carbon environments within the probing region. The narrowing of the G peak with increasing precursor size is evidence for preservation of the C–C bonds within the PAH framework, leading to stronger van der Waals interactions and π-π stacking within the final material.

Table S1. Structural properties of all materials investigated herein, as determined using XRD, Raman spectroscopy, N_2 adsorption at ~77 K, combustion analysis, and electrochemical lithiation.

	XRD			Raman Spectroscopy		N_2 Adsorption	Combustion Analysis	Electrochemical Lithiation
	d_{002} (Å)	L_c (Å)	L_a (Å)	Pos(G) (cm^{-1})	FWHM(G) (cm^{-1})	BET SA ($m^2\ g^{-1}$)	H:C (molar ratio)	Total Li Capacity* (mAh g^{-1})
Ben800	3.58	11	21	1594	72	16	0.11	219
Nap800	3.57	12	20	1597	70	21	0.11	292
Pyr800	3.47	19	20	1590	82	5	0.14	281
Cor800	3.42	22	18	1600	53	4	0.20	297
AG20	3.35	314	43	1564	20	9	0.00	320
ZTC	-	-	-	1592	60	3330	0.20	255
Super P	3.54	21	41	1583	103	59	0.01	265

* - reversible low-rate (25 mA g^{-1}) GCD capacity, measured as the average of the 15^{th}-20^{th} delithiation cycles

12. Electrochemical Characterization of PAH-Derived Carbons

Analogous electrochemical characterization to that performed for the primary materials of interest (as shown in **Figures 2-3** in the main text) was also carried out for the series of PAH-derived carbons with increasing size from Ben800, Nap800, and Pyr800 to Cor800. Reversible CV scans measured at a scan rate of 0.1 mV s^{-1} (~0.2 C) are shown in **Figure S6a**. An increase in the relative intensity of the turbostratic intercalation event at ~0.1 V is observed. This is attributed to the increase in crystallite size and decrease in d_{002} as a result of improved stacking order imparted by the larger precursors. Interestingly, only Cor800 exhibits the unique redox event present at ~0.5 V vs Li/Li^+, attributed herein as "hydrogen-type" sites. The

specific discharge capacity under GCD cycling of each PAH-derived carbon is shown in **Figure S6b**, as a function of increasing current rate. An increase in reversible capacity as a function of increasing precursor size is observed at all current rates explored in this work.

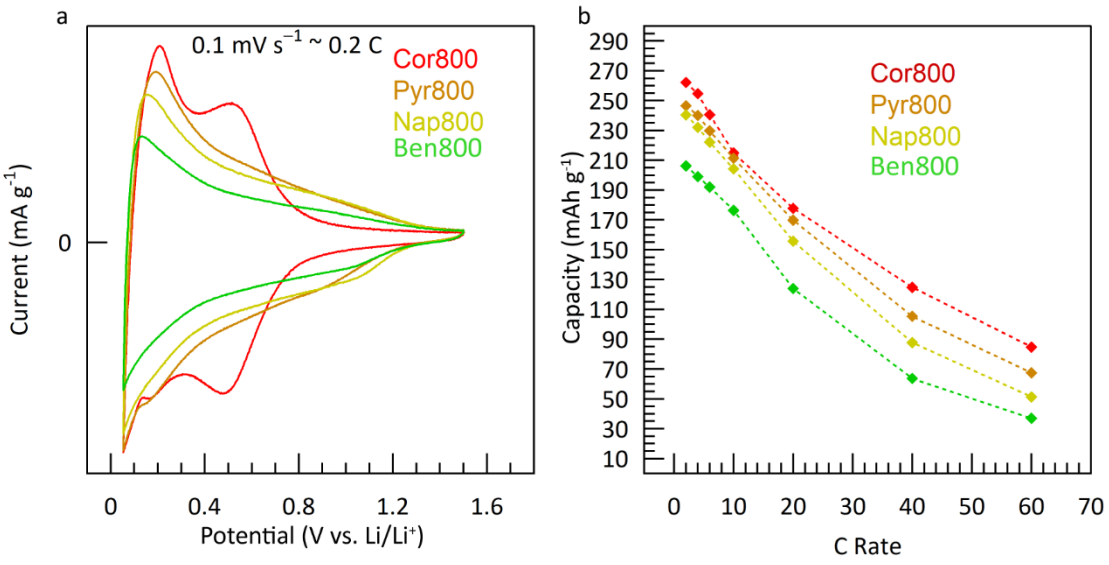

Figure S6. (a) CV profiles (at a 0.1 mV s^{-1} scan rate) and (b) GCD rate capability (between 0.4-30 A g^{-1} or ~1-60 C) of Ben800, Nap800, Pyr800, and Cor800.

13. Further Electrochemical Characterization of Primary Materials

The first cycle CV profiles of the four primary materials in this study, AG20, Cor800, ZTC, and Super P; at a scan rate of 0.02 mV s^{-1} are shown in **Figure S7a**, starting at open-circuit voltage (OCV, ~3.4 V vs. Li/Li^+) and cycling down to 0.05 V, then returning to 0.4 V. The relative magnitude of the solvent-accessible surface area of each material can be observed by noting the total current upon reduction from OCV to 0.05 V. It is remarkable that Cor800 shows only negligible current associated with the formation of solid-electrolyte interphase (SEI) during the first cycle, further confirming the confined nature of its "hydrogen-type" sites. The reversible CV profile of each primary material between 0.05-0.4 V vs. Li/Li^+ is shown in **Figure S7b**, at the same scan rate of 0.02 mV s^{-1}. AG20 exhibits distinct redox events that correspond to

the formation of staging compounds. All three other materials appear to exhibit similar CV profiles, making it difficult to discern between wide interlayer intercalation and capacitive adsorption in this range.

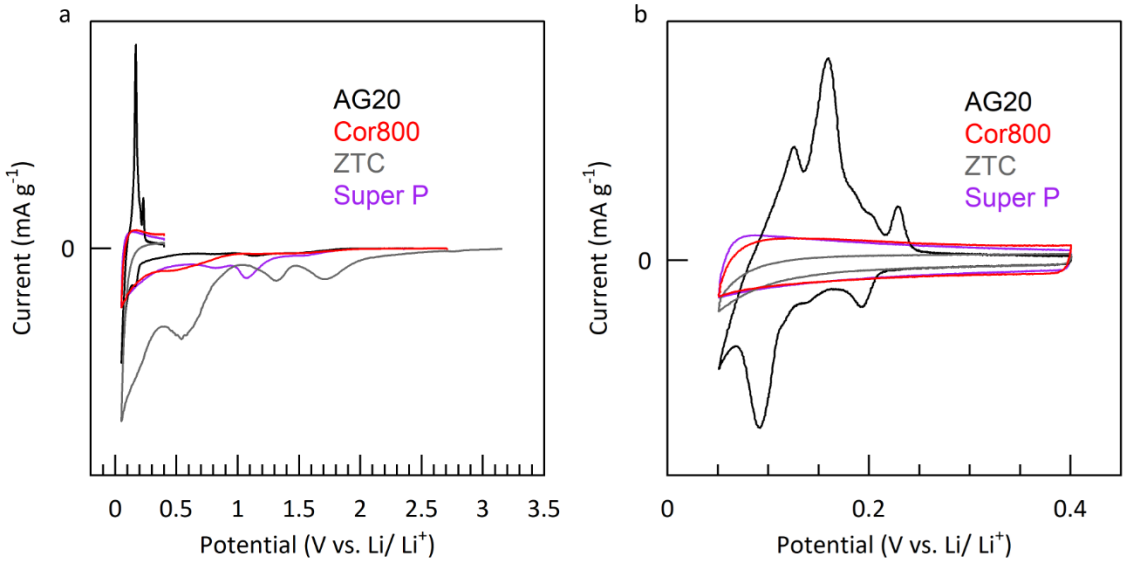

Figure S7. CV profiles (at a 0.02 mV s^{-1} scan rate) of AG20, Cor800, ZTC, and Super P between 0.05-0.4 V vs. Li/Li^+ (a) during the first cycle and (b) after extended cycling.

14. Supporting References

(1) Langford, J. I.; Wilson, A. J. C. Seherrer after Sixty Years: A Survey and Some New Results in the Determination of Crystallite Size. *J. Aappl. Crystallogr.* **1978**, 11 (2), 102-113 https://doi.org/10.1107/S0021889878012844

(2) Ferrari, A. C.; Basko, D. M. Raman Spectroscopy as a Versatile Tool for Studying the Properties of Graphene. *Nat. Nanotechnol.* **2013**, *8* (4), 235–246. https://doi.org/10.1038/nnano.2013.46.

(3) McGlamery, D.; Baker, A. A.; Liu, Y.-S.; Mosquera, M. A.; Stadie, N. P. Phonon Dispersion Relation of Bulk Boron-Doped Graphitic Carbon. *J. Phys. Chem. C* **2020**, *124* (42), 23027–23037. https://doi.org/10.1021/acs.jpcc.0c06918.

(4) Diana, N.; Yamada, Y.; Gohda, S.; Ono, H.; Kubo, S.; Sato, S. Carbon Materials with High Pentagon Density. *J. Mater. Sci.* **2021**, *56* (4), 2912–2943. https://doi.org/10.1007/s10853-020-05392-x.